II. Earthshine and the Earth's Albedo: Observations and Simulations Over Three Years

A [1,2], B[2], C[3] and D[3]

[1] U1

[2] U2

[3] U3

Contents

Received _____; accepted _____

ABSTRACT

Subject headings: Earth : albedo, global climate — Moon: reflection

Since late 1998, we have been making sustained measurements of the earth's reflectance by observing the earthshine from Big Bear Solar Observatory (BBSO). Further, we have simulated the earth's reflectance – for both the parts of the earth in the earthshine and the whole earth. The simulations employ scene models of the earth from the Earth Radiation Budget Experiment (ERBE), simulated snow/ice cover and real-time satellite cloud cover data.

Broadly, the simulations and observations agree. However, there are important and significant differences. The simulations show a more muted seasonal variation, which points to an inadequate treatment of the clouds.

During the rising phase of the moon, we measure the world to the west of California; while during the declining lunar phase, we measure the world to the east. Somewhat surprisingly, the 1/3 of the earth to the west and that to the east have virtually indistinguishable reflectances, inspite of the fact that the topographies look quite different. The part to the west shows less stability, presumably because of the greater variability in the asian cloud cover.

To determine a global albedo, we integrate over all lunar phases. Various methods are developed to perform this integration, but all give consistent results. Despite sizeable variations in the reflectance from night-to-night and season-to-season, which arises from changing cloud cover, we use the earthshine to determine annual mean albedos to better than 1%.

The earthshine observations provide an instantaneous, large-scale, precise determination of the earth's reflectance. As such, these measurements are an important complement to satellite determinations.

1. Introduction

In (REFERENCE), hereafter Paper I, we have detailed our method of determining the earth's reflectance from photometric observations of the bright (moonshine) and dark (earthshine) parts of the lunar disk. We have demonstrated that we can measure the large-scale reflectance of the earth to a precision of about 2% on any given night. Here we discuss the results of more than three years of observations of the earthshine. In addition, we have simulated the reflectance of the earth, treating separately the parts in the earthshine and all the earth in the sunshine throughout the hours of the day. In the simulations, we use scene models of the earth from the Earth Radiation Budget Experiment (ERBE) and real-time satellite cloud cover data. We discuss and compare the observational results with those of the simulations. Further, the seasonal changes in the earth's reflectance are contrasted and compared for the observations and the simulations.

On any one night, we determine the reflectance of most of the sunlit earth for a particular phase of the moon (the effective albedo). As detailed in Paper I, we need to integrate over all phases of the moon to determine a global or Bond albedo for the earth,

$$A = \frac{2}{3}\int_{-\pi}^{\pi} d\theta A^*(\theta) f_L(\theta) \sin\theta, \tag{1}$$

where A^* is the effective albedo associated with a particular night, $f_L(\theta)$ is the moon's Lambert phase function and A is the Bond albedo.

As described in detail in Paper I, the effective albedo is calculated from the earthshine measurements using

$$A^*(\beta) = \frac{3}{2f_L}\frac{p_b f_b(\theta)}{p_a f_a(\theta_0)}\frac{I_a/T_a}{I_b/T_b}\frac{R_{em}^2}{R_e^2}\frac{R_{es}^2}{R_{ms}^2}, \tag{2}$$

where $\frac{I_a/T_a}{I_b/T_b}$ is the ratio of the earthshine intensity to the moonshine intensity in two opposing fiducial patches, after each corrected for airmass. The ratio between the geometrical reflectivity of the two opposing fiducial patches, $\frac{p_b}{p_a}$. The lunar phase function for the bright side, $\mathrm{f}_b(\theta)$, is used in the formula to account for the geometrical dependence of the reflectivity of the moon, while $f_a(\theta_0)$ accounts for the fact that the earthshine is not exactly retroflected from the moon ($\theta_0 \lesssim 1^\circ$).

For convenience, the measured earth's albedo is often expressed as the magnitude of the effective albedo, A*, i.e.,

$$[A^*] = -2.5 \log A^*. \tag{3}$$

This standard astronomical definition implies that the larger $[A^*]$ is, the smaller the albedo. Note that a 1% change in A^* corresponds to a about $0^m.01$ change in $[A^*]$.

Each night, we observe 10 fiducial patches, 5 on the Crisium side, and 5 on the Grimaldi side (see Figure 3 in Paper I). In principle, we obtain 25 values of [A*] from the 25 combinations of the 5 pairs of fiducial patches. This gives us a way to evaluate the reliability of our measurement of [A*]. Figure 1 (a) and (b) shows the [A*] plot – morning (moon's phase decreasing toward new) and evening (moon's phase increasing toward full) – against lunar phase for the mean of the 25 datasets for each night. It is clear that the same pattern of variation appears in all datasets, indicating that this pattern is real and not from measurement noise. We take an average of the 25 measurements of [A*] for each night as shown in Figure 1 (c), and the standard deviation of the mean in [A*] is calculated as 0.016 and 0.018 for morning and evening respectively, yielding a measurement accuracy of better than 2%. In detail, we calculated the $\sigma^2 = \frac{\Sigma_i([A^*]_i - [\overline{A^*}]_i)^2}{N-1}$, where N=5 and i=1-25.

So far, observational data have been accumulated for more than 40 months covering the winter of 1998-1999 through the early 2002 (1998 December 9 - 2002 March 31). We also have 73 nights of data from 1994 January 7 - 1995 August 4, which will be discussed in Paper III of this sequence (REFERENCE). Both the instantaneous [A*] variation during each single night, and the variation of the nightly average [A*] throughout the seasons, have been obtained and compared to the simulated results using a scene model, snow/ice cover data and satellite cloud cover data.

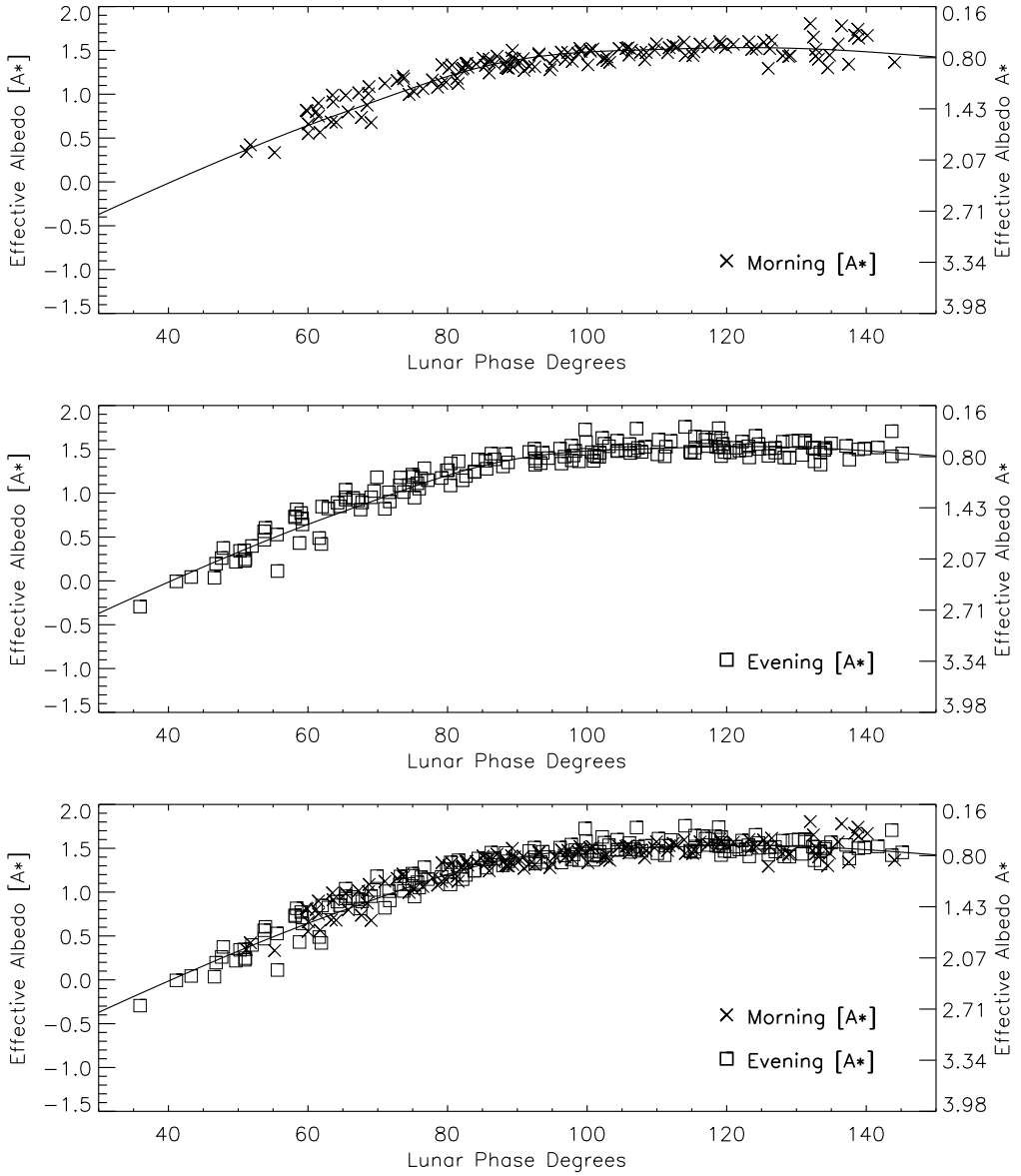

Fig. 1.— Plot of the mean $[A^*]$, which is determined from 25 sets for each night, for (a) morning and (b) evening observations. Panel (c) gives the combined results for mornings and evenings. In the figure, 340 nights of observations are included (150 nights of morning observations and 190 evening). The dark solid line in all panels indicate the curve from the fit to the data in the bottom panel, as described in §6. On the right hand y-axis, we use units of A^*.

2. The Observed $[A^*]$'s during 1999-2001

Figure 1 illustrates the change in $[A^*]$ against lunar phase as determined from the nightly earthshine observations – with the morning and evening observations presented separately, and combined. In the plots, each data point represents a nightly averaged $[A^*]$ value, with which we study the changes in $[A^*]$ for different nights, months and seasons. One may first note that while $[A^*]$ is relatively flat near the quarter moon, it sharply decreases as the full moon approaches. The flatness of implies a near-Lambertian earth for most phase angles (see Equation (9) of Paper I), but at small phase angles, the decrease implies that the earth looks relatively shinier due to enhanced reflectivity at grazing angles (glint). For lunar phase magnitudes much below about 40°, we presently regard the results as unreliable because of the proximity of the earthshine fiducial patches and the terminator (the transition from the moonshine to the earthshine is not sharp). Further, we do not have reliable earthshine data near the new moon (much beyond a lunar phase magnitude of about 140°) because the earthshine is visible for only a brief time near sunset or sunrise, depending on whether the moon is in its waxing or waning phase. Thus, the extrapolation to zero airmass is unreliable. For large phase angles, it is also difficult to find a fiducial patch that is confined to the moonshine.

A detailed examination of Figure 1 reveals that, with respect to the fitted mean, the $[A^*]$ determined from the local BBSO morning observations (lunar phase > 0) are not apparently distinct from those determined from the local evening observations (lunar phase < 0); i.e., the earthshine data from BBSO nights implies that the contemporaneous sunlit parts of the earth are equally shiny in the evening and in the morning (ultimately, in §6, we determine from the earthshine data a mean albedo of 0.2925 ± 0.0026 for the evenings and of 0.2957 ± 0.0023 for the mornings). The lack of a significant difference may seem somewhat surprising because the earthshine we observe in the mornings and in the evenings comes from the reflection of sunlight from different parts of the earth. In our evening observations, the earthshine is dominated by southeast Asia. In the mornings, the earthshine is dominated by Africa, Europe and the Atlantic.

Bearing in mind that a change in $[A^*]$ of $0^m.01$ corresponds to about a 1% change in A^*, we

observe a roughly ±5% night-to-night variation in the earthshine, A^*, even near the quarter moon where the data are most reliable. This variation is primarily associated with night-to-night changes in the cloud cover, rather than some error in the data collection/reduction process. In Figure 1, the spread about the mean is even larger, and we shall see that this is primarily associated with seasonal variations (§6.4) in the reflectance, Goode et al. (2001).

To better understand the influence of the earth's varying topography and cloud cover on $[A^*]$, we plot the albedo as observed throughout single nights in Figure 2. This plot comes from using Equation (2) after each point is corrected for airmass, and inputting the proper lunar phase for each observed time point. Note that the lunar phase function changes by about 1° per hour. In Figure 1, each point represents the mean of a single night. In each panel of Figure 2, the mean for the night is given as a number. In Figure 2a and Figure 2b, observations of two nights with almost the same lunar phase, but from different months are compared. Both observations were made in evening at BBSO (as opposed to the early morning). They demonstrate a common tendency of an early decrease in $[A^*]$, or a brightening earth, as the sun is rising over Asia, increasing the contribution from the relatively bright Asia, although the trend is more apparent in Figure 2a. The sun rising over a cloudy Asia causes a 5-10% change in A^* over the period of the observations. Even though the temporal evolution of the points in Figures 2a and 2b closely resemble each other, the mean value of A^* in Figure 2a is 5% smaller. This difference reflects a greater Asian cloud cover on March 24 than July 20. As we shall see in §6, some part of the appreciable difference is due probably due to seasonal changes in cloud cover, rather than differences in the part of the world we are measuring. In Figures 2c and Figure 2d, the observations are from two mornings at similar phases of the moon, and covering comparable local times. One notices immediately, that the A^* in Figures 2c and 2d are about 10% smaller that their counterparts in 2a. In Figures 2c and 2d, each panel shows an increasing $[A^*]$, or a darker earth, as time goes on. This is because the sunrise over the Atlantic is increasing the role of the darker, and less cloudy, ocean in the earthshine.

As shown in Paper I for one night, if we combine nights to obtain, say, a seasonal average,

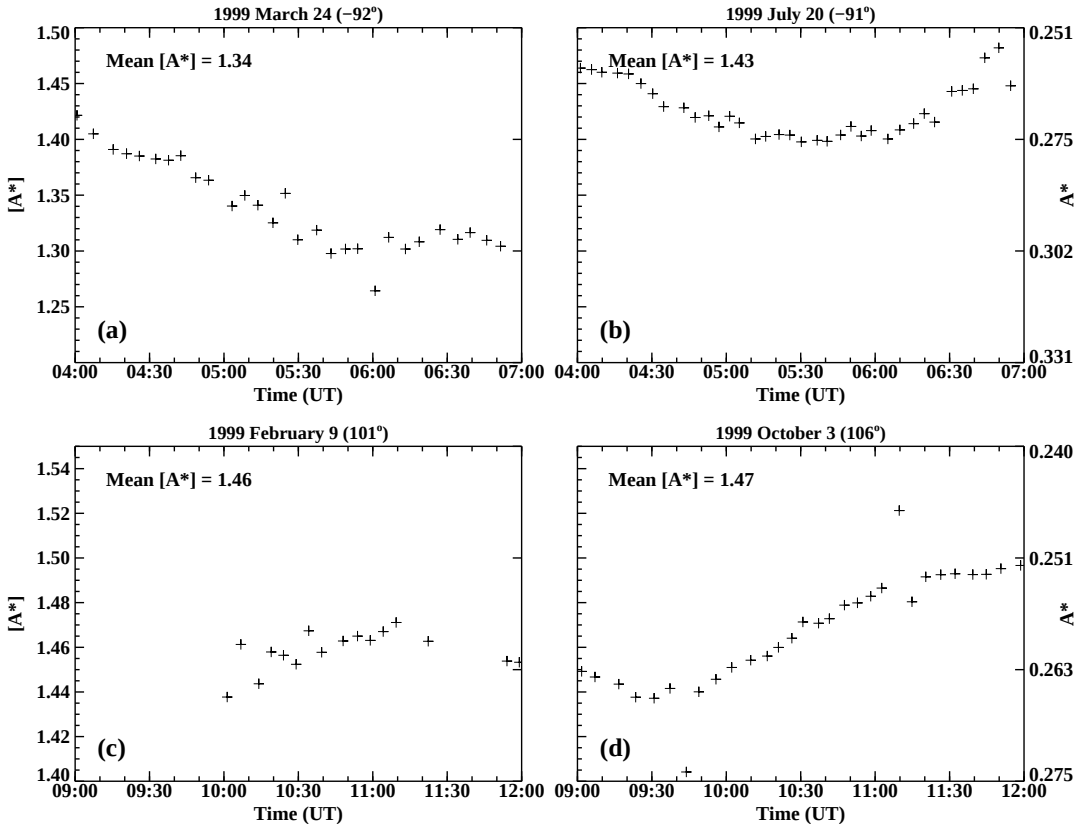

Fig. 2.— Plots of $[A^*]$ observed in the night of (a) 1999 March 24, (b) 1999 July 20, (c) 1999 February 9, and (d) 1999 October 3, against the time of observations. The right y-axis gives the result in units of A*. The values are derived for the fiducial pair used in Goode et al. (2001) and as indicated in Figure 3

then the total deviation will be smaller, but no smaller than that associated with the mean values of the various lunar phase functions and the ratio of the geometrical albedos. For instance, we have 340 nights of data for which the fit to Beer's Law has a standard deviation of less than 1% for the single pair of fiducial patches of Figure 3, as used by Goode et al. (2001). We regard these as our "good" nights. If we calculate the standard deviation of the mean for the 150 (190) mornings (evenings) pairs, we find 0.8% (0.7%). Combining this with the uncertainty in the lunar phase, we find an deviation of less than 1% in the binned A^*'s. Such error bars would be well-within the symbols of Figure 1. The most likely source of systematic errors is the determination of the geometrical albedos, coming from a single lunar ecilpse, but such systematic errors would not change the spread in the points. If the presumed systematic errors were comparable to the measurement errors we can reasonably identify, they are still considerably smaller than the spread in the $[A^*]$'s that appear in, say, Figure 1.

3. Modeling the Observations

In principle, we have the information to determine a Bond albedo from the simulations by using scene models of the earth, and adding cloud cover data from satellites and snow/ice cover from models. However, a precise determination is no easy matter. In general, the Bond albedo is given in terms of the albedo of each element of the earth's surface by,

$$A = \frac{1}{\pi R_e^2} \int d^2R (\hat{R} \cdot \hat{S}) a, \tag{4}$$

where d^2R is an element of the earth's surface, $\hat{R}$ is a unit vector pointing toward the local zenith, and $\hat{S}$ is a unit vector pointing toward the sun. The albedo of each surface element, a, depends on the surface type, cloud and snow/ice cover and solar zenith angle. The integral is over all portions of the globe illuminated by the sun (i.e.,$(\hat{R} \cdot \hat{S}) \geq 0$). However, to compare the simulations with our observations, we have to consider the ratio of the earthlight to sunlight, Γ that would be seen by an observer on the moon.

There is a systematic variation of Γ throughout the lunar month. When the moon is nearly new (lunar phase $\theta \approx \pm\pi$), the earth is nearly full, and so Γ is relatively large ($\approx 10^{-4}$). Conversely, when the moon is nearly full ($\theta \approx 0$), the earth is a thin crescent and Γ becomes vanishingly small. Fluctuations of Γ about its systematic behavior are caused by varying terrestrial conditions, including weather, the seasons and climate change. The lunar phase, θ is defined in Figure 2 of Paper I. After correction for the dependence of the reflectivity on lunar phase, one obtains

$$\Gamma = \frac{1}{\pi R_{em}^2}[\frac{R_{ms}}{R_{es}}]^2 \int_{(\hat{R}\cdot\hat{S},\hat{R}\cdot\hat{M})\geq 0} d^2R(\hat{R}\cdot\hat{S})a(\hat{R}\cdot\hat{M})L, \tag{5}$$

where $\hat{M}$ is the unit vector pointing from the earth toward the moon, and the integral is over all of the earth's surface for which the sun and moon are simultaneously above the horizon (i.e., $\hat{R}\cdot\hat{S}$ and $\hat{R}\cdot\hat{M} \geq 0$). The anisotropy function, L, generally depends on surface type, cloud cover, and the zenith angles and relative azimuth of the sun and moon. L is defined so that it is unity for a Lambert surface (see Equation (7) in Paper I). In terms of Equation (9) of Paper I,

$$A^* = \frac{3}{2f_L}\Gamma\frac{R_{em}^2}{R_e^2}\frac{R_{es}^2}{R_m s}, \tag{6}$$

because Γ is the ratio of the earthshine to moonshine intensity that would be seen by a lunar observer, there is no dependence on lunar reflectivity.

3.1. The Models

In modeling the reflectance properties, a and L, of the earth, we used scene models developed for the Earth Radiation Budget Experiment (ERBE) observations (Settles, et al. 1988). Twelve scenes are tabulated, varying from "desert" (areas for which the annual precipitation is less than 26 cm) to "mixed land-ocean" areas which are cells bordered by two land and two ocean cells. For the snow/ice cover, we used simulations from the Canadian Center for Climate Modelling and Analysis (CCCM II, `http://www.cccma.bc.ec.gc.ca`). This Gaussian grid is roughly $3.8^\circ \times 3.8^\circ$ in longitude and latitude. The model gives the monthly mean snow/ice cover for each grid cell.

The simulations of the earth's albedo were performed using two different cloud cover data sets.

Our primary dataset for the model calculations is uncalibrated images of the global cloud cover produced by the Weather Services International (WSI) Corporation. We use these data in the simulations of our observations. The WSI Corporation is the only place we know of that is currently producing real-time, on-line publication of global cloud cover maps. WSI maps (`http://www.intellicast.com`) are composed of data from both geostationary and polar orbiting satellites, including: GOES7, GOES8, METEOSTAT 5 and POES. Data from multiple orbits are mosaicked together to provide wide-scale global and full earth views in a single image. To allow for continuous night and day viewing of cloud patterns, infrared imagery is used. We download and calibrate daily WSI images.

For studies covering the previous solar cycle in Paper III, we use the D2 revised algorithm (Rossow, 1996) monthly mean fractional cloud cover data from International Satellite Cloud Climatology Project (ISCCP). The presently released ISCCP dataset covers 16 years over the period January 1984 through December 1999. We have used these calibrated data on a square grid which is $2.5° \times 2.5°$ degrees in latitude and longitude. The ISCCP dataset makes use of visible and infrared radiances, total cloudiness is determined using both of them, whereas other cloud types are determined using infrared radiances only. It has a spatial resolution of 280 km^2 cells and the cloud fraction in each of them determined by dividing the number of cloudy pixels by the total number of pixels per cell.

ISCCP was established as part of the World Climate Research Program (WCRP) to collect and analyze satellite radiance measurements to infer the global distribution of clouds, their properties and their diurnal, seasonal, and inter-annual variations. Data are collected from the suite of weather satellites (including NOAA, METEOSAT, GOES-EAST, GOES-WEST, GMS satellites) operated by several nations and processed by several groups. All ISCCP data products are archived at the ISCCP Central Archive (`http://isccp.giss.nasa.gov`).

Whereas ISCCP cloud data is given in percentage cloud coverage, the WSI images we download from the web are given in arbitrary units and it is necessary to translate them into

fractional coverage. The daily WSI images, are each placed on a "T42" square grid ($2.8^\circ \times 2.8^\circ$) and so is ISCCP data. We make use of the "T42" square grid because this is the format for snow and ice data, albeit of one of the most common formats for climatological data. We have made WSI monthly mean cloud cover maps (values are in arbitrary units), and compared them with the ISCCP monthly mean maps (in units of fractional cloud cover). Primarily we are looking for completely overcast areas, we find for those areas the minimum number of counts in the WSI images, and assign 100% cloud cover for any number of counts equal or greater to this mimima. We also look for clear sky scenes and we assign a maximum number of counts in WSI images below which we consider them to be 0% cloud cover. The values between the maxima and minima are converted to percentage coverage units using a simple polynomial parametrization. This yields an empirical non-linear calibration curve between the two cloud datasets, by which WSI arbitrary units are converted into ISCCP fractional coverage, although this does not translate into a one-to-one correspondence between the two datasets. As we will see in following sections, important differences between the two still occur. The use of a different calibration curve can altogether increase or decrease the mean albedo, but cannot increase the muted seasonal variations derived from the models. We emphasize that there is *no* inter-calibration between the model reflectances and those determined from our earthshine observations.

3.2. Model Results Covering 1999 -2002

In Figure 3, we show daily mean global albedos from our simulations of the whole earth covering 1999.0-2002.3, and calculated using Equation (4). Roughly, the figure shows peaks in the earth's reflectivity in the fall and spring, while showing minima in the winter and summer (see §6.4). From this, we determine a mean Bond albedo of 0.3001 ± 0.0002 over that period.

Applying Equation (6), we also simulated the earthshine observations shown in Figure 1 covering *the same parts of the earth at the same time*. The results are shown in Figure 4. Note that the distribution is tighter to the fit than in Figure 1. Thus, the greater scatter in Figure 1 cannot be due to different nights for the same lunar phase seeing different parts of the earth

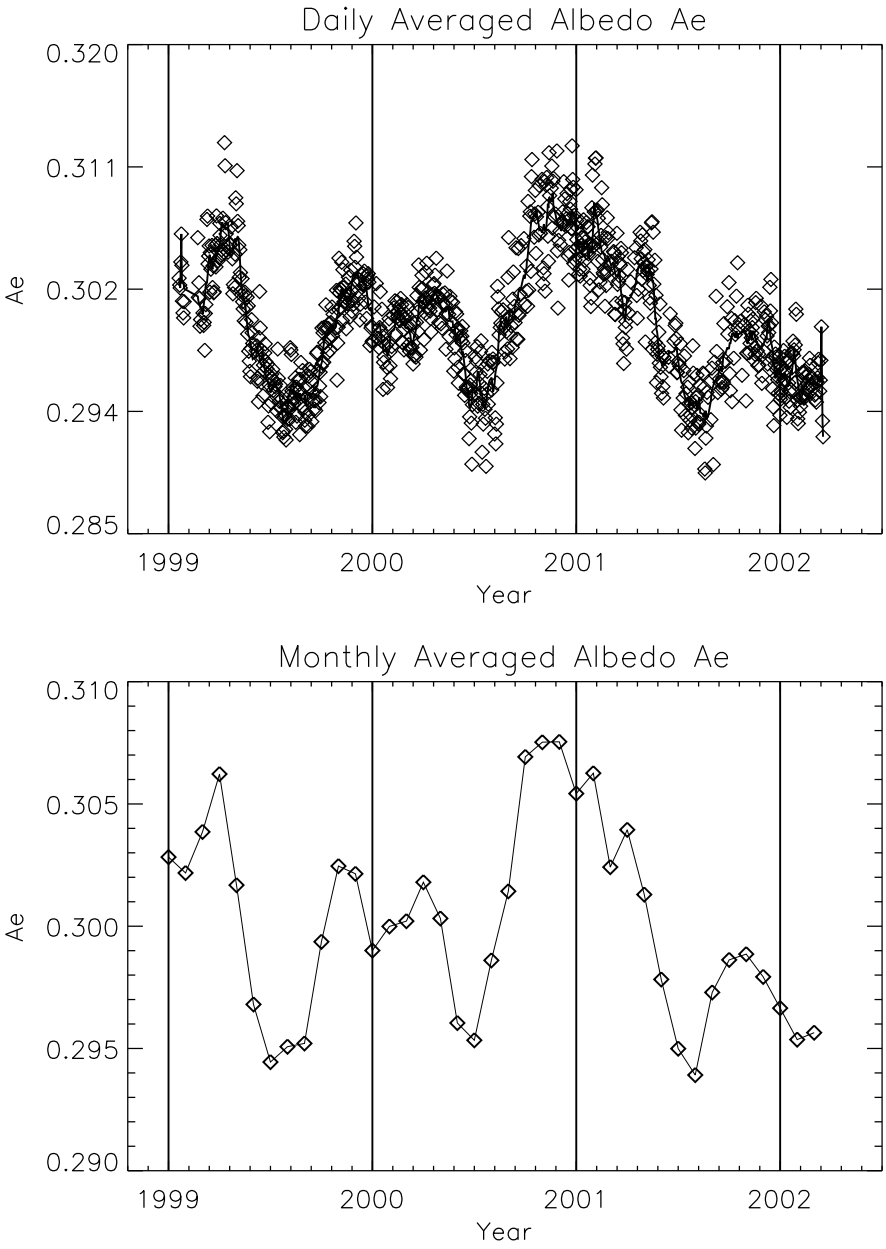

Fig. 3.— Top: Daily mean global albedos (diamonds) from the simulations beginning from January 1999 to March 2002. The albedo is calculated from snow and ice data from the Canadian Center for Climate Modeling simulations and WSI cloud satellite data, and includes the 24-hour albedo from all sunlit parts of the earth, whether visible from the moon or not. The bold solid line shows the 30-day running mean. The amplitude of the simulated seasonal variation of the whole earth albedo is 4-5%. Bottom: as in top panel but daily means are averaged into monthly means.

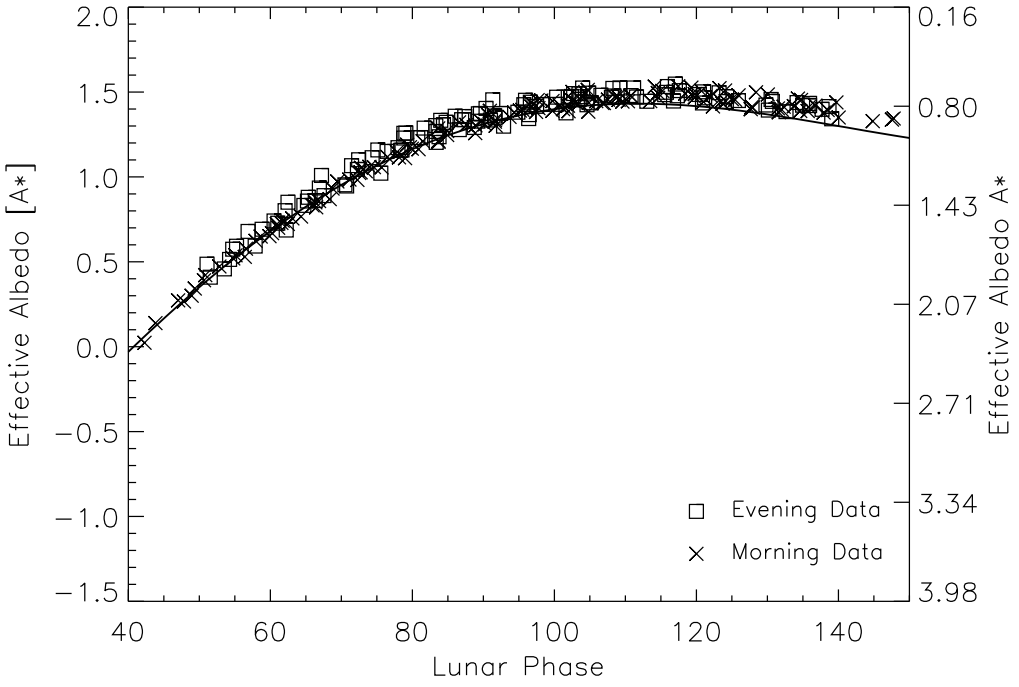

Fig. 4.— Plot of [A*] vs. absolute value of the lunar phase from simulations covering the same phases of the earth as the observational results in Figure 1, i.e., the simulations are looking at the regions of the earth visible from the moon at the times of our earthshine observations. Each data point represents the averaged [A*] value throughout one night; an "x" indicates morning observation (lunar phase > 0) and a "square" indicates evening observation (lunar phase < 0). For reference, the solid curve shown is fit to the data in Figure 1.

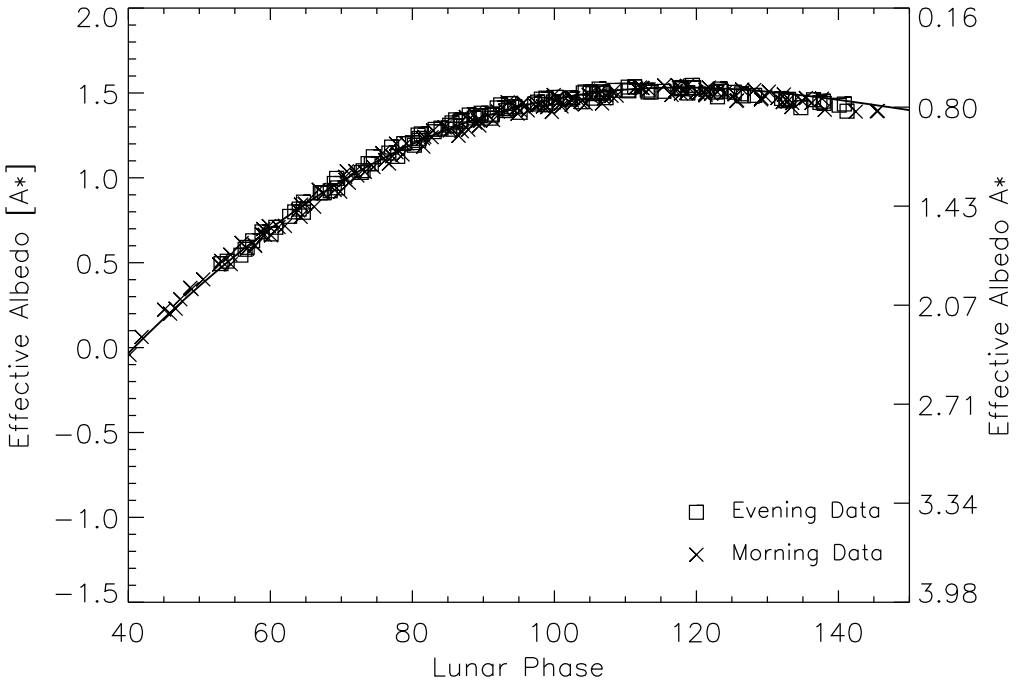

Fig. 5.— Plot of [A*] vs. absolute value of the lunar phase from simulations covering the whole earth for all days for which we have observations. Each point represents the 24-hour average of UT defined days for which we have earthshine data. The "x"'s and "squares"'s are given to show whether the 24-hour average is connected to observations at positive or negative lunar phase. For reference, the solid curve is the fit to the data shown in Figure 1.

because each night's simulation covers exactly the parts of the earth which are observed. We shall return to the origin of the difference in the spread in §4. However, like the observational results, there is no clear distinction between the simulations for day and night. As in Figure 1, it is also clear from the simulations shown in Figure 4 that the evening data have a greater scatter about the mean than do the morning data. This implies a more variable cloud cover over Asia. In Figure 5, we show the same kind of plot as Figure 4, but covering the entire earth for nights for which we have observations and cloud cover data (see the difference in coverage between the solid lines and solid boxes in Figure 6). Since the whole earth simulations average more of the globe, it is not a surprise that these simulations show considerably less scatter than those of a part of the earth. We also note that the mean effective albedo in our simulations, $[A^*]$, is lower for the whole earth than it is for the part we see by 0.016 ± 0.017 (1.3%) in A^*, i.e. the albedo increases when we add the third of the earth invisible to Big Bear. That may be a consequence of including the american land mass, although the result is not statistically significant.

3.3. Comparing Daily Observations and Model Results

In Figure 6, we show evening and morning earthshine observations overlaid on model calculations covering the entire day. The two lower panels show the earthshine as a function of time (note that the time is plotted in reverse chronological order). The solid curve shows the variation of the calculated effective albedo A^* during the twenty-four hour period, and the solid boxes are the observed effective albedo. These results come from near to a quarter moon and are compared with the earthwide WSI cloud cover from the same day in the top panel.

The top panel shows the cloud cover maps illustrating which parts of the earth contributes to the earthshine. We highlight (the large bright areas) those parts of the earth that are the source of the earthshine (i.e., are simultaneously in the sunshine and are visible from the moon at some time during the observations). The cloud cover is also shown as secondary grayscale, for instance, the east-west dark bands just north and south of the equator illustrate cloudless areas. We also indicate with boxes an intersection of the earth's surface with the bisectrix of the spatial angle

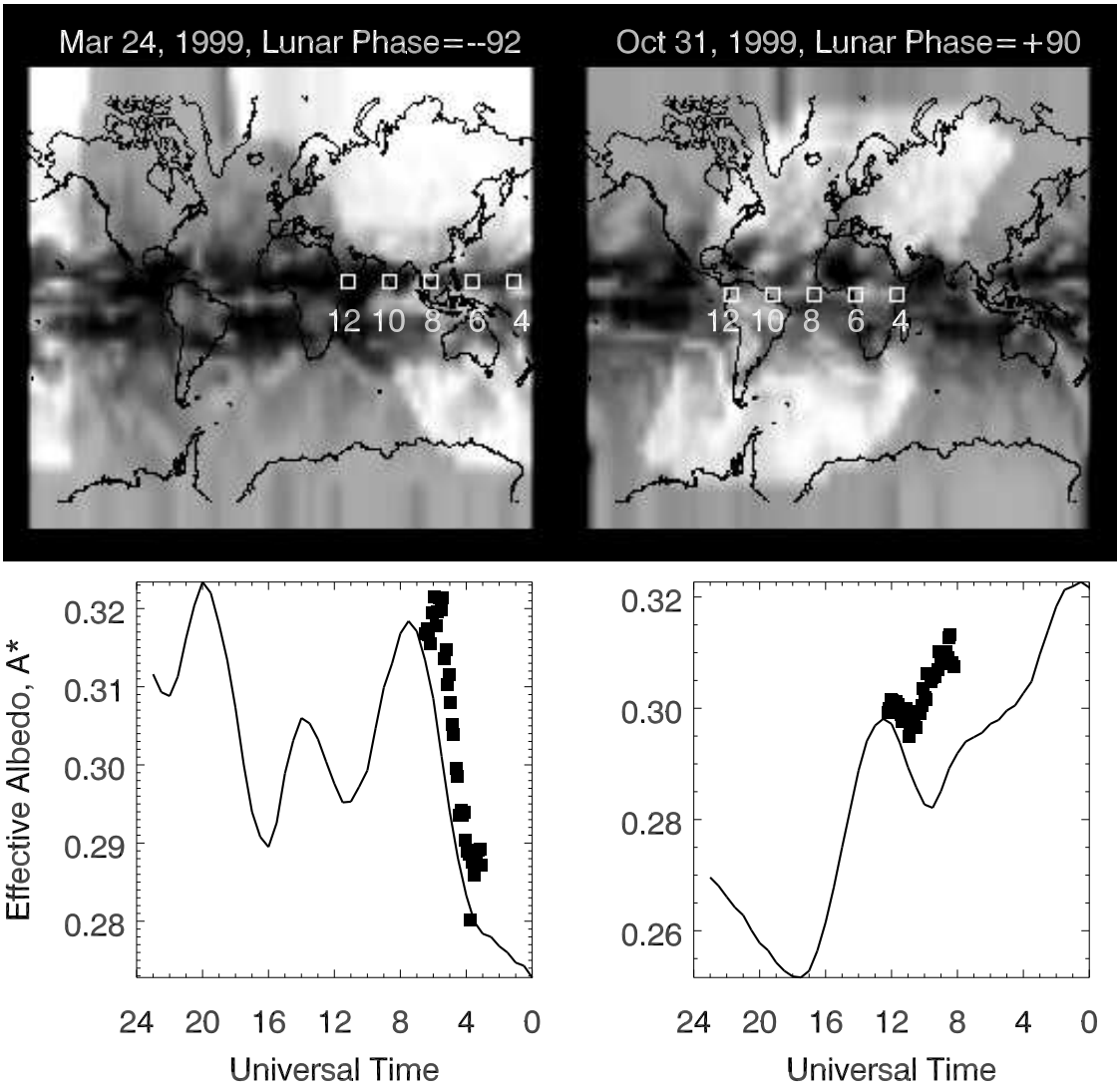

Fig. 6.— In the top panels, the extended bright areas highlight those parts of the earth that are the source of the earthshine. The satellite-derived WSI cloud cover maps are shown in a secondary gray-scale with brighter areas indicating greater cloud cover. For 31 October 1999, note that the northernmost regions are not sunlit and the southernmost regions do not contribute to earthshine because the moon is fairly far north in the sky. The empty white boxes in the top panels indicate the longitudes of maximal contribution to the earthshine at the Universal Time (UT) shown. The solid boxes in the lower panels show the observed effective albedo as a function of time (note that the time axis is reversed), while the solid line indicates the simulated A^*.

between the surface intersection of the lines from the center of the earth to the moon and the sun or, in other words, the point of equal angles, where the angle of incidence is equal to the angle of reflection.

The observations are consistent with the simulations for 24 March 1999, which is one of the nights for which the agreement is quite good. On 31 October 1999, a more typical night, there is a discrepancy of about 5% relative (or 0.015 absolute) in the effective albedo. One may notice slight, and opposite, temporal offsets between the simulations and observations in the lower panels. One must bear in mind that the cloud cover data are a composite of many observations which are taken over about six hours (and sometimes up to 24). Thus, a precise timing between the observations and simulations is not possible. We simply assume that the cloud cover is invariant from one posting to the next and we make no effort to smooth the transition. If there were a rapid cloud formation or movement, it could result in observational and simulated results which don't have the same form.

At high geographical latitudes above 45°, the cloud cover is fairly steady. Thus, the short timescale variations in reflectance in Figure 6 are due to primarily to irregularities in the fractional cloud cover at low latitudes and secondarily to the scene type. In the lower left panel of Figure 6, one sees that the observed and calculated maxima in A^* at 7:00 UT are due to a relative cloud excess over the Far East, while the calculated local minimum in A^* at 11:00 UT arises from the cloudless area above India and the Arabian Sea. In the lower left panel, there is a more than a 10% change in A^* over about two hours. This sharp increase is due to the increasing contribution of a cloudy Asia to the earth's reflectance as the earth rotates. An offset between the observed and calculated effective albedos is evident in the lower right panel. Typically, the observed results vary more about the mean than do the simulated ones. The larger variation in the observed results is a consequence of the less muted seasonal variations than predicted using the models.

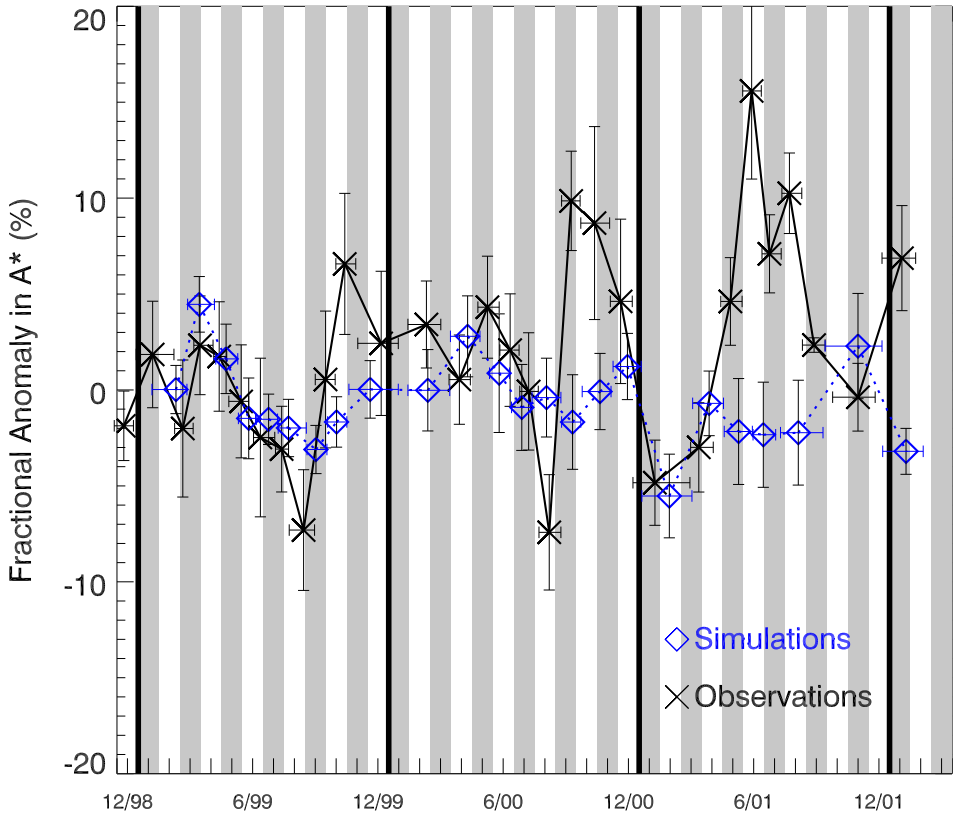

Fig. 7.— Seasonal anomalies in the effective albedo, A^*. From December 1998 through March 2002 , there are 340 nights of observations with 10 nights in each of the bins. From January 1999 onward, there are 268 nights for which we have both observations and contemporaneous satellite cloud cover data, which have been averaged in 24 bins with 10 nights in each. The $\times$'s show the mean of the observations, with the vertical bars being the standard deviation of the mean. The size of the latter stems from the large night-to-night variations in the cloud cover, rather than from uncertainties in the observations. The horizontal bars indicate the temporal span of each average. The diamonds indicate the corresponding simulation results. Anomalies are with respect to the mean for 1999.

4. Seasonal Averages of [A*]

The seasonal variation of the earth's reflectance is not well-known. In fact, Goode et al. (2001) have shown that over a year and a half (1999.0-2000.5) that the earth's seasonal variation was upward of 20%. This surprisingly large value is twice that determined from the simulations covering the same nights and the same parts of the earth. The formulation of the simulations was detailed in the previous section. Large scale, seasonal variations can be well-determined from the earthshine. Starting from Equation (2), the fractional seasonal variation depends only on the observed intensities corrected for airmass. That is,

$$\sum_{i=1}^{N} \frac{A^*_{\rm seas}(\theta_i) - \overline{A^*}(\theta_i)}{\overline{A^*}(\theta_i)} = \sum_{i=1}^{N} \frac{(\frac{I_a/T_a}{I_b/T_b}\frac{R_{em}^2 R_{es}^2}{R_{ms}^2})_{\rm seas,i} - \overline{(\frac{I_a/T_a}{I_b/T_b}\frac{R_{em}^2 R_{es}^2}{R_{ms}^2})_{\rm i}}}{\overline{(\frac{I_a/T_a}{I_b/T_b}\frac{R_{em}^2 R_{es}^2}{R_{ms}^2})_{\rm i}}}, \tag{7}$$

where N is the number of nights for which we have data in a particular season, θ_i is the lunar phase on the i^{th} night of that season, and $\overline{A^*}(\theta_i)$ is the fit shown in Figure 1. The average for a particular season is computed from each night's data by determining the fractional change for that night's phase angle with respect to the mean for that phase angle for all nights, irrespective of season. With this formulation, possible systematic errors associated with the moon's geometric albedo have been largely eliminated. In the formulation of Equation (7), we minimize the dependence on lunar phase by removing effects, in the mean, arising from the fact that A^* is a strong function of lunar phase. These seasonal anomalies, which are formulated as fractional changes in A^*, carry information about variations in weather, climate and surface type. The fractional seasonal variation of the earth's reflectance over three years (1999-2001), as determined from our earthshine observations, is shown in Figure 7.

As in the whole earth simulations in Figure 3, one can see in Figure 7 a clear seasonal trend for 1999 and 2000, with the earth being brightest in the spring and fall generally, when it is also the cloudiest (by WSI satellite data). We see the seasonal trends in spite of the fact that the night-to-night variations are a significant fraction of the seasonal trends. We emphasize that the large vertical error bars arise from the large night-to-night variations in the cloud cover, rather

than any errors in the data (see also Figure 1). In fact, the night-to-night variations are large compared to the formal error bars for one night (which are within the symbols in Figure 1). With all of this, we see about 15-20% variation in A^* from season-to-season. However 2001 does not show the same seasonal pattern. In the early months of the year, it shows a dip in the albedo that is also visible in the simulations, and it has a maximum in summer time, although this is not visible on the simulations.

The observations show about twice the variability as the simulations, with the differences being greatest at the extremes. The seasonal variation of albedo is the essential origin of the relatively greater spread among the observed $[A^*]$'s in Figure 1, as compared to Figure 4. The muted seasonal amplitude of the simulations may well derive from the coarse binning of the scene models and/or the use of simulated snow and ice cover. But the treatment of the clouds is a stronger candidate. Our model contemplate only 13 different scenes and 4 cloudiness levels (0-5%,5-50%, 50-95% and 95-100%). Beyond the appreciable binning of the cloud cover, changes in cloud type will also affect the albedo, but it is not accounted for in the models. We note that the whole earth seasonal simulations in Figure 3 show an even more muted seasonal variation (of the order of 5%). This is no surprise considering the relative spreads about the mean in Figures 4 and 5.

5. Comparisons with Danjon's Results

To compare our results with those of Danjon, we show our data in Figure 8, but analyzed using Danjon's phase function (as shown in Figure 14 of Paper I). In Figure 8, the solid line shown is the fit from Figure 1, which is for the same nights, but analyzed with the correct phase function. Clearly, for phase angles below 100° the data tend to lie above the fit, while for phase angles above 100° the point tend to lie below the fit. To understand why Danjon found a Bond albedo about 0.1 larger than the true value, one must also inspect the kernel from which the Bond albedo is determined, see Figure 9, where the kernel peaks at about 130° (near the quarter moon). These phases are most significant in the determination of the albedo. Thus, the inconsistency

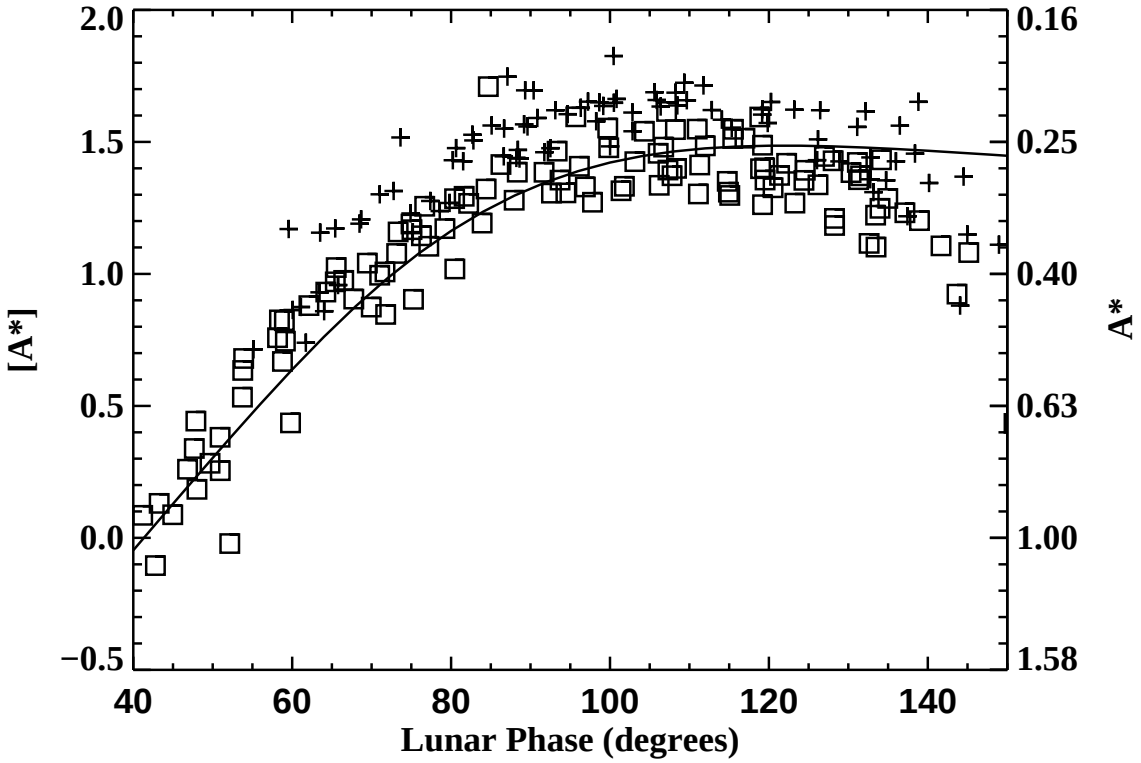

Fig. 8.— Danjon's lunar phase function (see Figure 14 in Paper I) was used to analyze our observational data. The solid curve is the regularized fit to the same data analyzed using *our* lunar phase functions, as in Figure 1. The points shown in this figure are those derived using Danjon's phase function. Since Danjon's phase function is systematically lower than the correct one for phase angles that make the largest contribution to A, this explains how Danjon derived an albedo of about 0.4 from his observations, which is much higher than our observed and simulated values of about 0.3.

between Danjon's albedo of about 0.40 and our observed value of 0.30 comes mainly from Danjon's underestimate of the lunar opposition effect (Flatte et al., 1991; MacDonald and Koonin, 1992), which carries over from the significant overestimate of the lunar phase function near the quarter moon that dominates the determination of the albedo.

6. The Bond Albedo

To determine the Bond albedo, A, from our earthshine observations we need to integrate $A^*(\theta)$ over all phases of the moon using Equation (1). The kernel of the integrand, $f_L(\theta)\sin\theta$, is plotted in Figure 9. The figure illustrates one of the two basic problems in using the earthshine to determine the earth's Bond albedo. The first, and more significant problem, is that we cannot measure the earthshine for all phases of the moon. However, it is clear from Figure 9 that this becomes a problem for determining A predominately for lunar phases near the new moon, where the earth is most nearly Lambertian. Further, it can be seen in Figure 9 that the integrand in Equation (1) peaks near the quarter moon ($|\theta| \sim 130^\circ$), when the moon shows a relatively sizable earthshine, while its phase is not so large that the earthshine is visible only briefly near sunset or sunrise. More precisely, to evaluate Equation (1) to an accuracy of 0.002 requires data for $|\theta| \geq 30^\circ$. Thus, earthshine observations for most lunar phases are needed for an absolute value of the albedo, while observations near the full moon are most sensitive to variations in the albedo because so little of the earth is visible. The second basic problem in using the earthshine to determine the albedo arises because the orbit of the moon traces out an ellipse in the full three dimension space surrounding the earth, so we cannot measure the earthshine in all directions. Therefore, we are insensitive to any azimuthal anisotropy in the earthshine. Later in this section, we use simulations to show that the effect of the anisotropy is not significant, but it is systematic and one can account for it. We do this by taking advantage of full spatial coverage provided by the simulations.

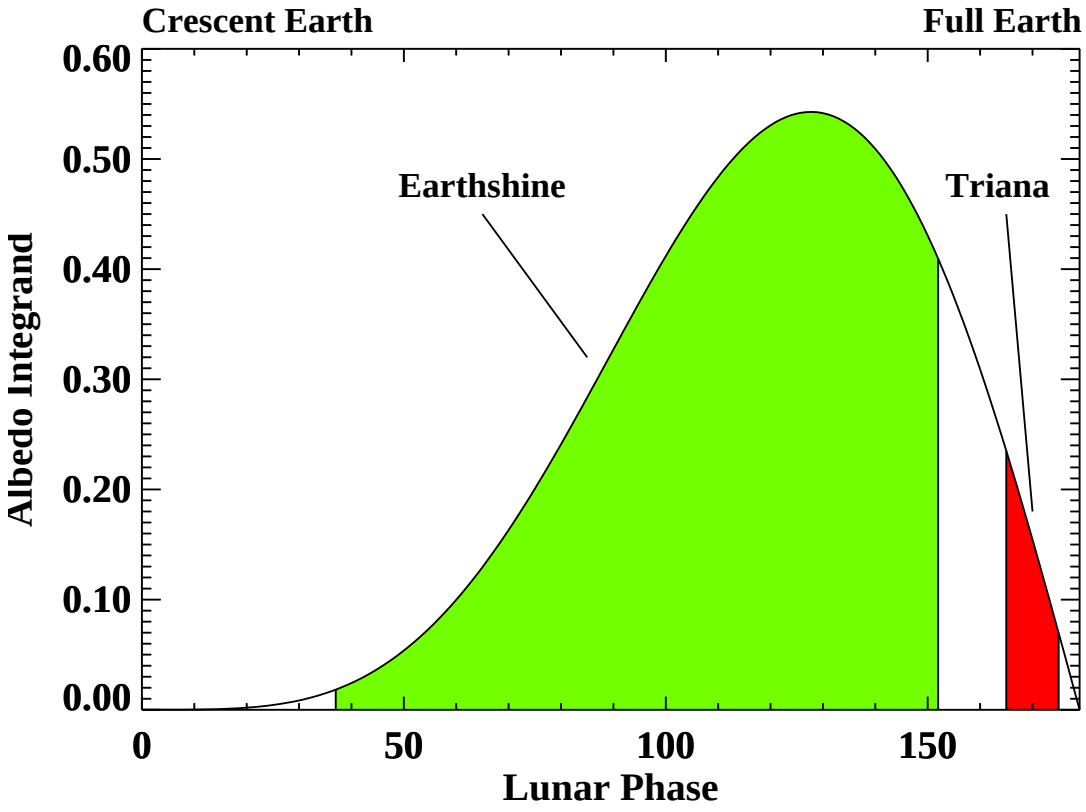

Fig. 9.— The kernel ($f_L(\theta)\sin\theta$) from which the Bond albedo is determined (see Equation 1) is shown as a function of lunar phase. Its behavior is dominated by the Lambert phase function for small phase angles, and by $\sin\theta$ for large phase angles. In green, we indicate contribution to the Bond albedo that arises the range lunar phases over which we measure the earthshine. In red, we show the approximate contribution from a satellite orbiting about L1, assuming the proposed orbit of Triana. If the orbit were to make larger loops around L1, as proposed by Lockwood (2002), all phase angles above 140° could be covered.

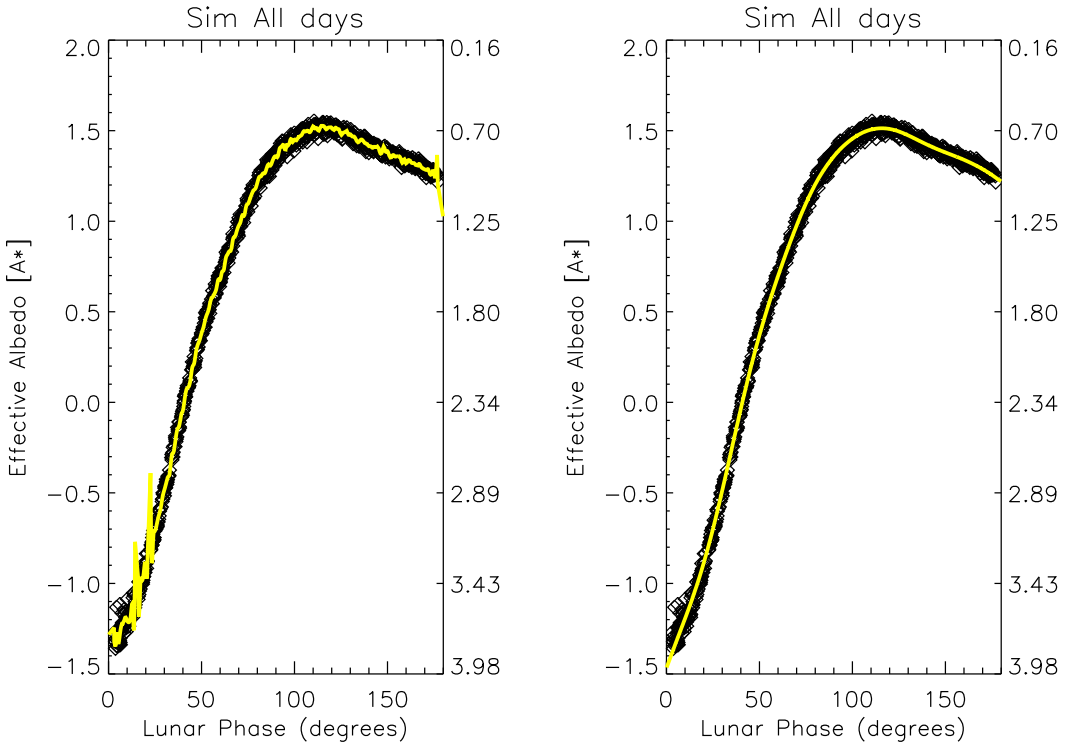

Fig. 10.— Each simulated, single night whole earth effective albedo is represented by an empty box. Since there are 898 nights, individual boxes cannot be resolved. The nights span the period from December 1998 to March 2002, and are the nights for which we have cloud cover data. Left panel: A least squares fit to the data is shown, with the effective albedo being determined in individual bins that are 1° wide. Note the short wavelength oscillations for all phase angles. Right panel: The regularized fit to the same data. On the right hand y-axis, we use units of A^*.

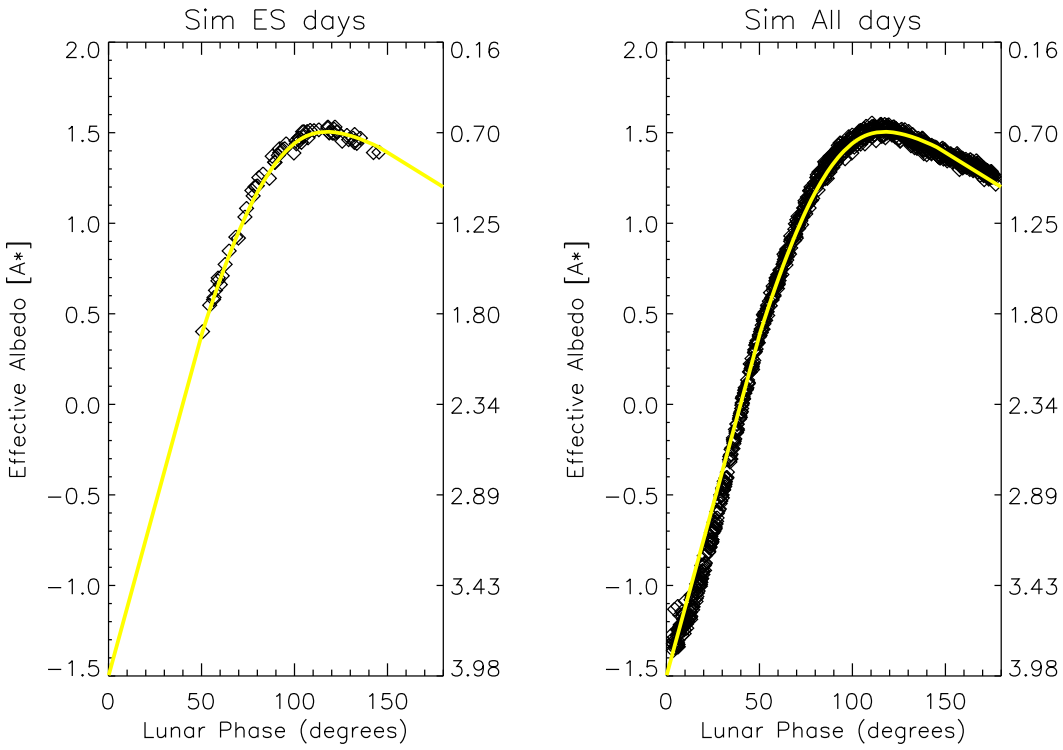

Fig. 11.— Each box represents a whole earth (i.e., covering a twenty-four hour period) simulated albedo. Left panel: Whole earth simulations for which the twenty-four hour period includes nights for which we have earthshine data and cloud cover (268 nights). The 268 nights span the period from December 1998 to March 2002. Right panel: Whole earth simulations for all twenty-four hour periods, during the same period, for which we have cloud cover data (898 nights – 466 during the waxing moon and 432 during the waning phase). The yellow curve in both panels is derived from the constrained or regularized least-squares fit to the left panel. On the right hand y-axis, we use units of A^*.

6.1. Determining A from A^*

We have a two-step approach to determining the Bond albedo from the earthshine effective albedos. The first step is utilizing the simulations. Simulations for the 3+ years of data for all nights that we have cloud cover are shown in both panels of Figure 10 (including all phase angles). The both the left and right panels show the same data. In the left panel, we show a least-squares fit in which the effective albedo is determined for 180 bins of 1° apiece. The least-squares fit is made using

$$\chi^2 = \frac{1}{(N - N_f)} \sum_{j=1}^{N} \left(\frac{\Delta A_j^*}{\sigma_j} \right)^2 , \tag{8}$$

where N and N_f are the number of nights simulated and the number of degrees of freedom in the solution, and where ΔA_j^* and σ_j are the deviation of A_j^* from the fit and the error in the determination of A_j^*, respectively. There are short wavelength oscillations in $[A^*]$, which are largest at the extreme phase angles. The extreme phase angles do not contribute to the Bond albedo, which is 0.2939±0.0001 for the least-squares fit. The short wavelength oscillations are an unpleasant artifact of the least squares method. We could, instead, perform a least-squares fit with a low degree polynomial, which would suppress the oscillations. However, the meaning of the stiffening would be unclear. We believe that the effective albedo should be a smoothly varying function, and we impose this in a mathematically meaningful way – regularization – in which we minimize

$$\chi^2(1 - \frac{N}{N_f}) + \lambda \int_{-\pi}^{\pi} [\theta^2 \frac{d^2}{d\theta^2} (\frac{\Delta A_j^*}{A^*})]^2 d\theta, \tag{9}$$

where ΔA_j^* is the difference between the j^{th} data point and the fit to the data (the quantity we are determining) in the right panel of Figure 11, while λ is the regularization parameter which is, in reality, a smoothing constraint. In principle, the parameter is adjusted until χ^2 per degree of freedom is unity, so that the errors in the data are converted to comparable errors in the fit. However, the χ^2 space is relatively flat, so one typically weakens λ until short wavelength oscillations almost begin to appear in the fitted A^* function. Other forms of the constraint are certainly possible, but a second derivative constraint seems to work best here. In applying the regularization to the right panel, we have the advantage of being able to directly compare the

obtained value of 0.2937± 0.0003 to that obtained by out simple least-squares (0.2939±0.0001). The two results are consistent, and known with about an order of magnitude greater precision than we have been discussing for the observations. The error in the Bond albedo from regularization is about three times greater than that from the least-squares determination. Still, the regularization introduces a point-to-point correlation in the errors, but we shall see that this effect is small and the errors very nearly take the standard meanings.

Next, we apply regularization to the subset of nights shown in left panel of Figure 11, and using essentially the same regularization parameter as in Figure 10, and after assuming the left panel and right panel have the same values at phase angles of 0 and 180°. The left panel is the subset of 24-hour simulations for which we have observational data taken on the same calendar day. The resulting fit is shown in both the left and right panels of Figure 11. It can be seen that the fit to the subset of the data fits the whole of the data quite well, especially for the range of phase angles that are so important in determining the Bond albedo. With this fit, we find a Bond albedo of 0.298±0.001, which we regard as being consistent with the pure least-squares and regularization results of Figure 10, after recognizing the fact that 2/3 of the nights in the right panel Figure 11 are absent in the left panel. The fit is fairly insensitive to the choice of λ over nearly an order of magnitude. For a review of regularization and its utility, see Goode (1995).

The second step in determining the Bond albedo for the observations is a further effort to account for the fact that the observational data do not span all phase angles. For this, we next examine the A* simulations for the daytime region of the earth visible from the moon, for phase angles between 60 and 120° – the regime for which we have the most confidence in the data. In Figure 12, we show a scatter plot of the Bond albedo for a twelve month running mean vs. the contribution to that integral coming from phase angles between 60 and 120°. To construct the 12-month running mean, we start from the period December 1998 to November 1999 and then remove the first month and add a new one until the period April 2001-March 2002. The correlation between the total and "partial" integration values is of 0.98. To test this method, we have repeated it using the interval 90-120 degrees and we get a correlation between total and

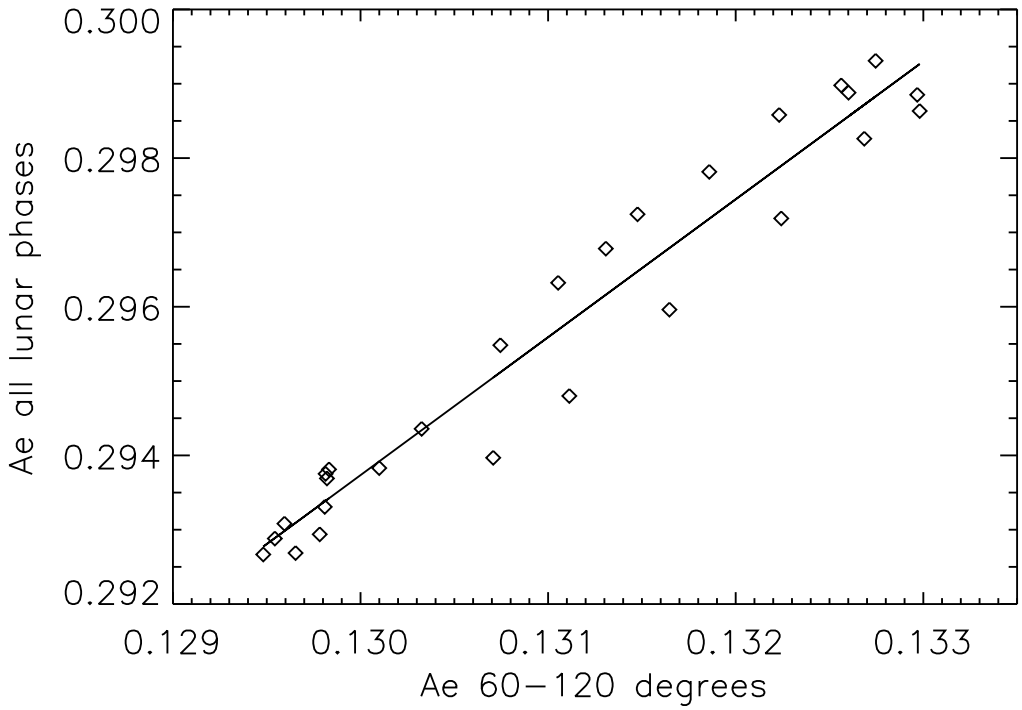

Fig. 12.— Correlation coefficient between total integration over all phases and partial integration between 60-120 degrees for a running 12-month mean of the whole earth simulations.

"partial" integration of 0.99. The linear fit gives us a way of converting a partial integral to a total integral. The albedos obtained by converting the partial integrals and from the total integrals are practically indistinguishable. After experimentation, we find that this approach returns more reliable values for the albedo than a simple regularization fit as used here in the left panel of Figure 11 and in Goode et al. (2001).

We next use this linear relation to determine a Bond albedo from the observational data. Again, we use the daytime earth's region visible from the moon simulation points at 0 and 180° to fix the regularization and then determine the Bond albedo by scaling the fit between 60 and 120° by the same linear factor as used in determining the Bond albedo for the simulations at all available lunar phases. Applying the same regularization to the observational data of Figure 1, which contains, as a subset, the 268 nights in the left panel of Figure 11, over a 3+ year period we find the mean Bond albedo for the earth to be 0.295±0.002 (0.2925±0.0026 for the evening observations and 0.2957±0.0023 for the morning). The deviations will contain not only the noise, but also any long term albedo variability that might have occurred during this period. The fit is shown in the the left panel of Figure 14. The right panel shows the corresponding fit for the simulations covering the same times and parts of the that contribute to the earthshine, for which we calculate an albedo of 0.298±0.001. The larger deviations in the observational results are indicative of the greater spread of the observational points about the mean (compare the left and right panels of Figure 14).

One of the prices paid using regularization is that the point to point values of the solution are correlated, implying that the meaning of the errors is somewhat damaged. The damage is reflected in errors that are smaller than they are in reality. For instance, if the constraint were dominant, the uncertainty at each point in the solution would be the standard deviation of the mean. To ascertain whether the uncertainties quoted in this section are significantly too small, we also determined the errors in a completely different way which does not suffer from the limitations imposed by regularization and reveals that they are not significantly too small (see §6 .4).

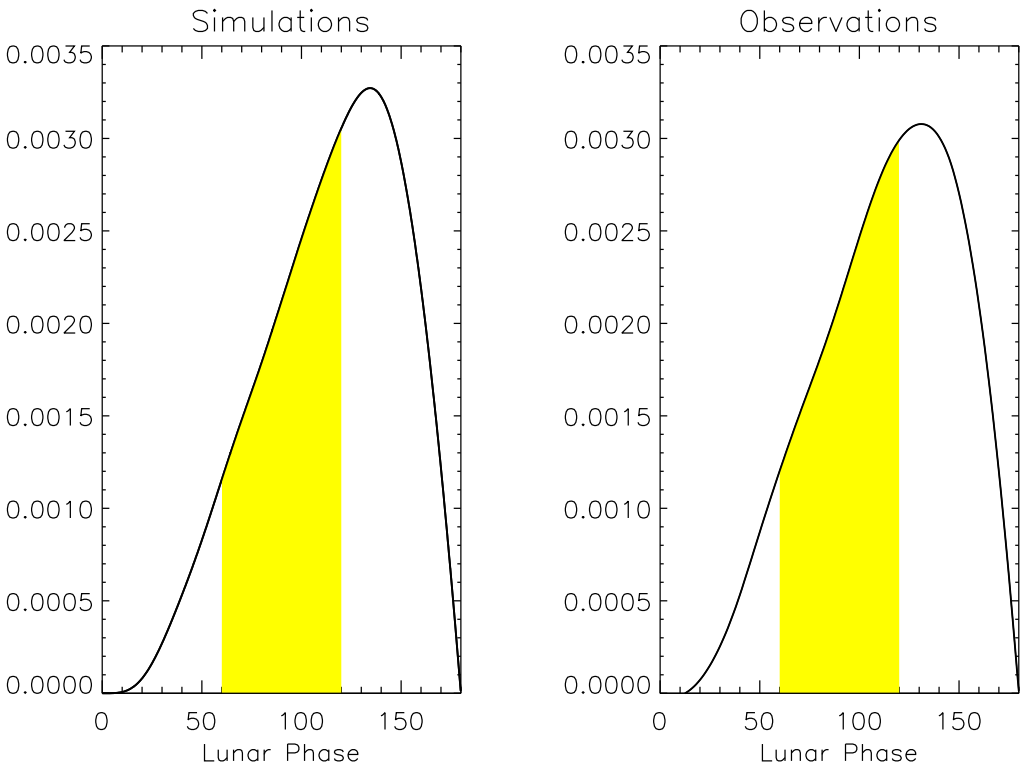

Fig. 13.— Left: The integrand of Equation 1 (kernel of Figure 9 multiplied by $A^*(\theta)$) using the 3+ years 24-hour simulations at all phases. Right: The same integrand using 3+ years of observational data. The area between 60 and 120 degrees is shaded in both figures.

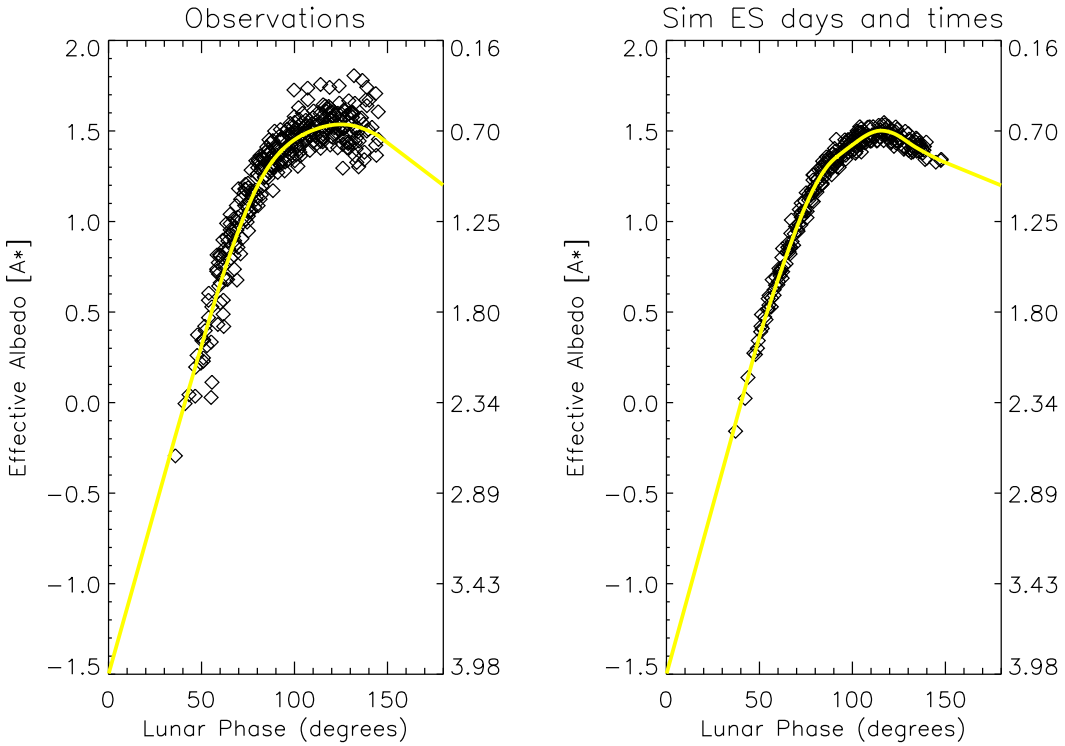

Fig. 14.— Observed (left panel) [A^*]'s plotted against the absolute value of the lunar phase from 225 clear observing nights from December 1998 through March 2002. Simulations (right panel) are shown covering the time intervals and parts of the earth that contribute to the earthshine signal for the 268 nights for which there were observations and contemporaneous cloud cover data. Each data point represents a nightly average of a series of 0.5-3.0 minute earthshine measurements taken once every five minutes with 0.1-5.0 second moonshine observations interspersed. Error bars for each night would be within the symbols. For the 268 nights for which we have observations and simulations, constrained least square fits to the data and simulations are shown by the yellow curves. On the right hand y-axis, we use units of A^*.

6.2. Effect of Anisotropy

As mentioned at the beginning of this section, one concern about measuring the earthshine to precisely determine the earth's albedo is the amount of anisotropy in the earth's scattering. At any instant, the moon subtends 0°.5 as seen from the earth, and the obliquity of the moon's orbit extends this coverage over the lunar month to only 6° on either side of the ecliptic; thus, earthshine is not sensitive to light scattered out of the ecliptic. We can directly test the sensitivity by comparing the result of simulating the Bond albedo for the *whole* earth to that using the simulated earthshine. For the case of the of the earth that is in the sunshine, we use Equation (4) and calculate an average for the more than three years of data, for which the result (A=0.3001±0.0002) is shown in Figure 3. For the whole of the earth in the earthshine, we are effectively assuming that for all lunar phases the earthshine does not depend on the azimuthal scattering angle. We test Equation (1) by using $A^*(\theta)$ from the least squares fit in the left panel of Figure 10 from which we determined an equivalent 3+ year average Bond albedo of 0.2939±0.0001. The discrepancy arises because the relatively brighter polar regions are sometimes in the sunshine, but not in the earthshine. For this reason the values obtained from our earthshine observations and our [A*] simulations should be increased by 0.006. This effect is illustrated in the right panel of Figure 6 for which the moon is northerly in the sky and doesn't receive light from the sunlit southernmost regions of the earth.

6.3. Precession of the Lunar Nodes

A higher order difficulty in determining the earth's reflectance from the albedo is that the intensity of the earthshine varies with the precession of the lunar nodes. That is, because the gravitational effects of the sun and moon are not always the same, there is some wobble in the motion of the earth's axis; this wobble, called nutation, causes the celestial poles to move, not in perfect circles, but in a series of S-shaped curves with a period of 18.6 years. This precession of the moon's orbital plane has a period of 18.6 years. The sensitivity of the earthshine arises

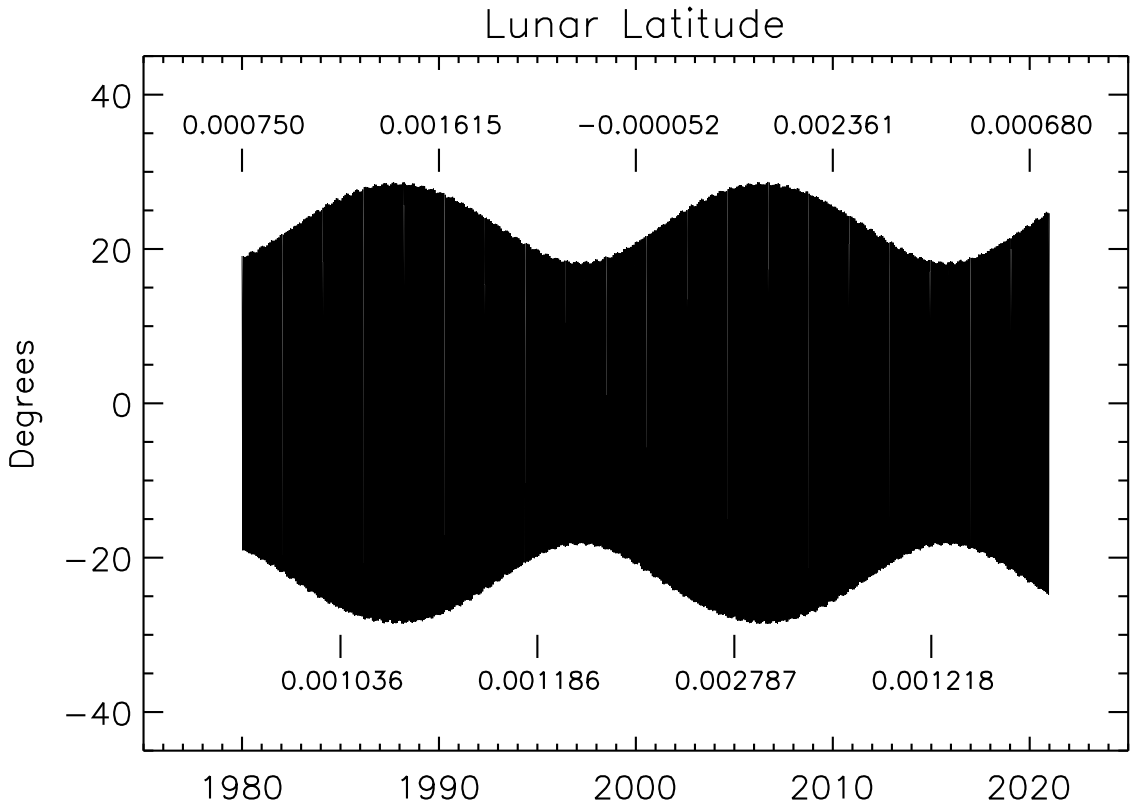

Fig. 15.— The precession of moon's orbital plane with a period of 18.6 years induces a corresponding periodicity in the earth's albedo. The figure shows simulations for the period 1980-2020, using 25th January 1999 cloud cover data as though all nights were "frozen" in time with the same cloud cover. Also indicated, for some of the years, are the mean annual changes in Bond albedo, with respect to the albedo for 1999, caused solely by the evolving lunar declination. The albedo was simulated using Equation (1).

from the anisotropy of the light scattered by the earth. For example, when the declination of the new moon is a maximum (some 29°), and it is near the northern-summer solstice, more of the arctic polar ice cap is visible and the earthshine will be brighter. Some nine years later, the lunar declination under the same conditions will be only 18°, and the earthshine will be a minimum. We have performed simulations to study this effect and the results appear in Figure 15 and the Table 1. It is clear from the figure that the nutation of lunar nodes perturbs $[A^*]$ at the $0^m.004$ level or less, or about five times smaller than the effect of anistropy. It is straightforward, but necessary to account for this in comparing earthshine results from different epochs.

6.4. Alternate Determination of Uncertainties in the Bond Albedo

In calculating the Bond albedo, we have an alternative way to connect the precision to which we determine the $[A^*]$ to the accuracy to which we determine A. To do this, we use the daily cloud cover maps and calculate the whole earth albedo A, the effective earth's albedo $[A^*]$ and the variation of each during the full day and during the times for which we have earthshine observations. For the calculations, we use a third-order polynomial fit to $[A^*]$, which defines a mean calculated effective albedo for the earth, $\overline{[A^*(\theta)]}$, and residuals, $\Delta[A^*]^{calc} = [A^*] - \overline{[A^*(\theta)]}$; these latter carry information about the weather, climate and surface type. Their correlation with the calculated global albedo anomalies ($\Delta A = A - \overline{A}$) at the times at which earthshine observations have been taken, is shown in the top panel of Figure 16, where we have included the 268 nights for which we have simultaneous cloud cover data and earthshine observations.

Table 1: Effects of the nutation of the moon's orbital plane comparing similar times (left) and different epochs (right)

N	Span of Years	A_e	$\Delta A_e/A_e$ in %
1	1996(jan) - 1998(mar)	0.29453	$[A_e(3) - A_e(1)]/A_e(1) = 1.1\%$
2	2002(jan) - 2004(mar)	0.29612	$[A_e(2) - A_e(1)]/A_e(1) = 0.7\%$
3	2008(jan) - 2010(mar)	0.29623	$[A_e(3) - A_e(2)]/A_e(2) = 0.3\%$

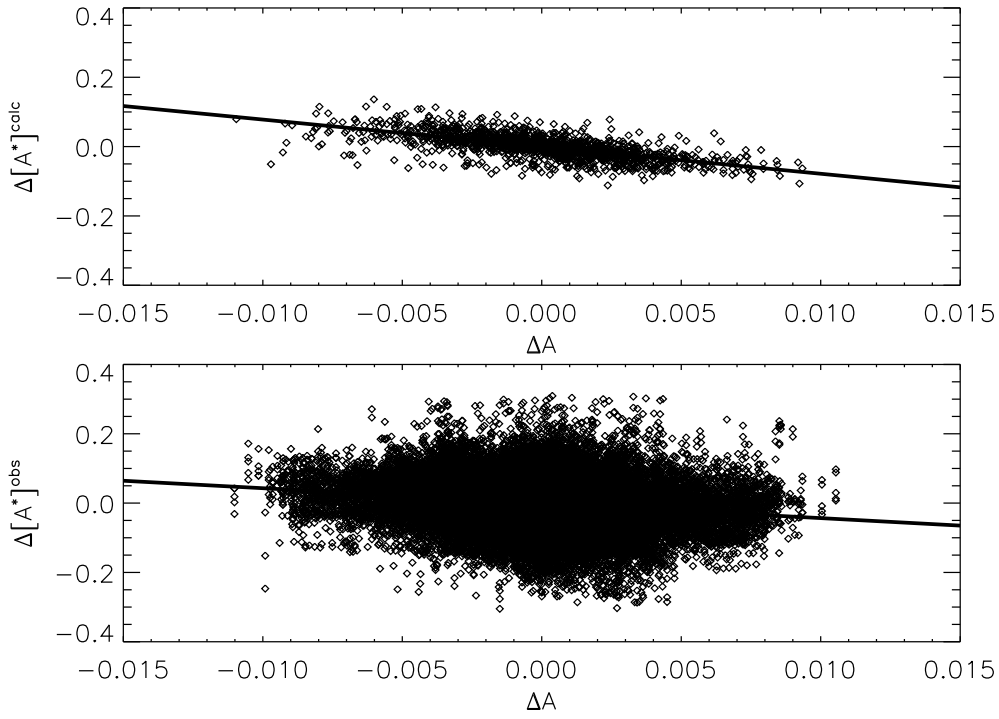

Fig. 16.— Top: Linear correlation of the calculated earthshine anomaly, $\Delta[\mathrm{A}^*]^{\mathrm{calc}}$, with the calculated global albedo anomaly, ΔA for 1694 calculations for lunar phase angles for which $140^\circ \geq |\theta| \geq 40^\circ$. Bottom: Linear fit to observational anomalies, $\Delta[\mathrm{A}^*]^{\mathrm{obs}}$, during the same time periods, assuming ΔA is the same as that from the calculations.

For the observational data, we make a scatter plot during the same periods, and assume they correlate with ΔA, as shown in the lower panel of Figure 16. In detail, we used a third-order polynomial fit to define a mean observed effective albedo $\overline{[A^*(\theta)]}$ and observed residuals $\Delta[A^*]^{obs}$. Their correlation with the global calculated albedo anomalies ($\Delta A = A - \overline{A}$) is shown in the lower panel of Figure 16 including a linear fit to the points. This figure gives us insight into how accurately we can measure the albedo. The largest number of points in the lower panel comes from the fact that in order to make a direct comparison, we interpolate our 30-minute resolution ΔA from simulations for each time at which an observation is taken (a period between 0.5-3.0 minutes). Whereas in the top panel, a direct comparison between ΔA and $\Delta[A*]^{calc}$ is done. The correlations are -0.66 and -0.27 in the top and lower panels respectively, both significant at higher than a 99.99% significance level.

Using Figure 16, we note that a variation in A of 0.01 corresponds to changes in $[A^*]^{obs}$ of $0^m.043$ (or 4.0% in the observed A^*, using $\delta[A^*] = \frac{\ln 10}{-2.5}\frac{\delta A^*}{A^*} = -1.08\frac{\delta A^*}{A^*}$) and to a change in $[A^*]^{calc}$ of $0^m.078$ (or 7.2% change in the calculated A^*). Equivalently, a 1% earthshine measurement of A^* determines the albedo with a precision of 0.0025. To place this precision in context, we note that independent satellite determinations of the monthly mean albedo can differ by 0.005 or more and that the seasonal range of the monthly mean albedo is 0.015 or more (see Figure 7). The individual simulated points have error bars of about 0.005 and the seasonal variations have an amplitude of 0.027. These values are close to those from satellite data.

Our nightly $\sim 2\%$ observational uncertainty in each nights measurement of A^* corresponds to a deviation in of $\sim 0^m.02$ $[A^*]$, which implies measuring A to ± 0.005. This value is comparable to that from satellite data. From the figure, we converted the error in $[A^*]$ into the error in A, which averaging over a year, implies measuring A to slightly better than 0.005 (or to about 0.003 over three years) – even though we have observed about a third of the nights in the year. These uncertainties are similar to those we determined using constrained least-squares for A. Thus, we conclude that the regularization has not underestimated the uncertainties in a meaningful way.

NEED REFERENCES IN THIS SECTION REGARDING SATELLITE MEASUREMENTS.

7. Mean Albedos from Different Cloud Cover Data

In Figure 7, we compared the seasonal variations of our observations with the corresponding variations in the simulations. Here, we reach further back in time to examine seasonal variations as determined from simulations. In the model calculations, we use monthly averaged cloud cover data from the International Satellite Cloud Climatology Project (ISCCP), which spans the sixteen year period from the beginning of 1984 through the end of 1999. We also have daily cloud cover from WSI spanning from January 1999 to present.

Figure 17 shows binned, monthly means of the earth's albedos calculated using the ISCCP (thin solid curves) and the WSI data (diamonds and boxes connected by thick lines). For the ISCCP data, the solid thick curve shows an average over the sixteen years monthly mean albedos. The thick broken lines show $\pm 1\sigma$ of this average. The error bar for each year is determined from the quality of the fit to the averaged monthly variation in the earthshine.

Figure 17 also shows an apparent difference between albedos obtained using different data sets. The WSI albedo is significantly lower than the ISCCP one. The computed averaged ISCCP albedo $\overline{A}$, is 0.313 and the WSI averaged albedo $\overline{A}$ is 0.300. This difference is well-within what we can measure. However, the recent release of new ISCCP data has give us our first year of coincidence between ISCCP and WSI cloud data, 1999. ISCCP data for 1999 is the lowest of all in albedo and cloudiness and so the offset between the two datasets in the common year is reduced by half (0.007).

The remainder of the offset probably arises from the use of monthly or daily means to calculate the albedo. Monthly albedos from the ISCCP data are calculated on the basis of mean monthly cloudiness maps, whereas for WSI the albedo is calculated daily and then averaged to form a monthly mean. Using only WSI data, we have learned that first averaging the cloud data into monthly means, and then calculating the albedo artificially increases the mean by an amount of between 0.001 and 0.006. This is consequence of the crude resolution of our albedo model in which cloudiness has only four possible values.

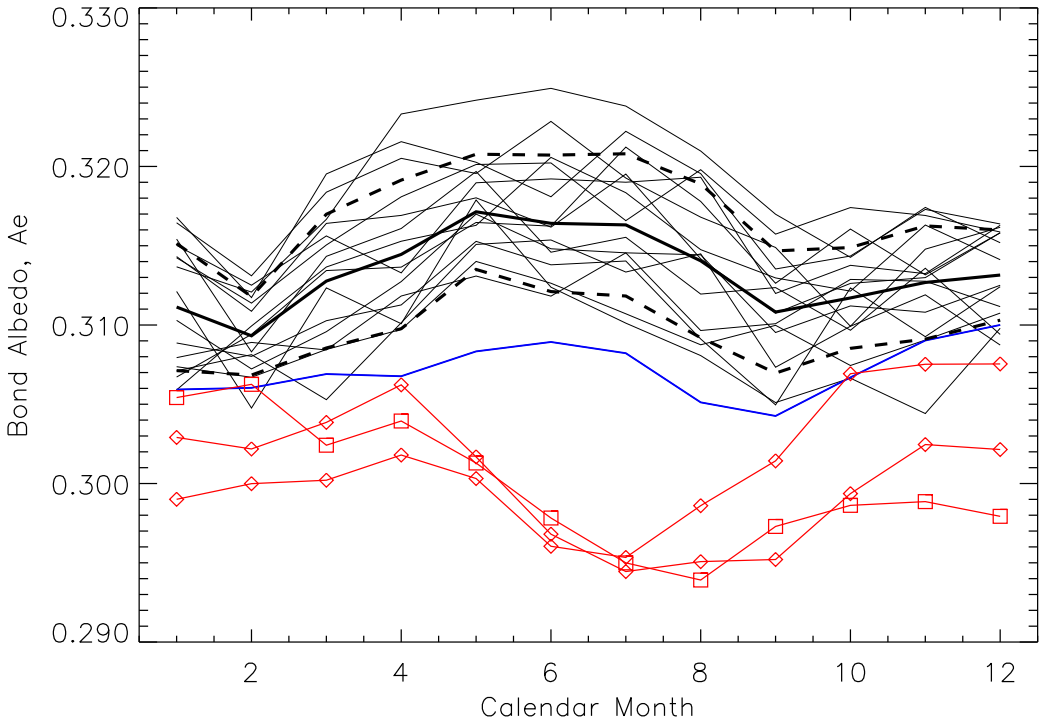

Fig. 17.— Comparison of albedos using different datasets. The WSI results for 1999-2001 are indicated by the lines which are connecting the diamonds and boxes. The ISCCP-D2 results cover 1984-1999 and are indicated by the band of light solid lines. The thick solid line is the mean of 1984-1999 and the dashed lines give the $\pm 1\sigma$ bands about the mean. The slightly thicker lower solid line and boxed line correspond respectively to data for the common year 1999 between the ISCCP and WSI datasets. The two sets have different seasonal variabilities, at least during the summer months (May-August).

We cannot explain the different seasonal cycle of the ISCCP and WSI cloud data (or deduced albedos). While the WSI simulations show the expected seasonal variation with an August minimum and November and May maxima (Danjon 1928; Dubois 1942; Dubois 1947), the ISCCP data has a more broad peak during the summer months, which generally increases the albedo for the year. The dominant source of the seasonal variability is the interplay of the annual cycle of snow/ice cover with the cloud cover; the greater land fraction in the northern hemisphere plays only a small role.

Even though ISCCP cloud cover data have been most carefully calibrated, the values derived from the more poorly calibrated WSI data are in good agreement with the satellite-derived Bond albedo value of 0.30 (Gibson et al. 1990; Rossow and Lacis 1990). It is probable then that the albedo estimations from the ISCCP data are overestimated (by an amount close to 0.007 judging from the observations and WSI simulations). We shall have an extended discussion on annual values and trends for the Bond albedo both from simulations and observations in Paper III.

In the future, a new calibration between the WSI and ISCCP data will be undertaken by a direct comparison of the available and forthcoming overlapping data. This will probably further reduce the offset between the sets of two simulations. Also, a distinction for different cloudiness levels (with different radiative properties) is available with the ISCCP data and will be included in our models.

8. Discussion

From BBSO, we have observed the earthshine for more than three years. We determined a large scale average of the earth's albedo for major areas the earth, including Europe, Africa and the Atlantic Ocean in our morning observations, when the sun is high over Africa and the Atlantic Ocean and the moon is in its declining phase. We also measured the albedo for large areas in southeast Asia and the Pacific in our evening observations during the rising phase of the moon.

We have compared our results with models of the earth's scenes inputting contemporaneous

snow/ice cover from models and cloud cover from satellites. We find a correlation between the observed and calculated results, with the calculated results uniformly showing milder amplitude seasonal variations. From this, we suggest that the models are overly smoothed. We argue that the earthshine data provide an important complement to satellite observations of the earth.

We have learned that the albedo we determine is as precise as determined from satellites, while providing an excellent complement. One of the obvious advantages of earthshine observations is having an absolute calibration coming from the bright side of the moon. A clear drawback of earthshine observations has been determining the lunar phase function – the reflection of light from the moon as a function of the phase of the moon. We have solved this problem, as demonstrated in Paper I, so that we know the standard deviation of the phase function to within 0.5%.

From the earthshine data, we see that southeast Asia and West Africa/Southern Europe have very nearly the same albedo. We also see that the albedo is the largest in the spring and fall.

REFERENCES

Danjon, A., 1928, Ann. Obs. Strasbourg, 2, 165

Danjon, A., 1954, in The Earth as a Planet, ed. Kuiper, p.726, Chicago

Dubois, J., 1942, Ciel et Terre, 58, 352.

Dubois, J., 1947, Bull. Astron., 13, 193

Flatte, S., Koonin, S., and MacDonald, G., 1991. in Global Change and the Dark of the Moon, JSR-91-315 (McLean, VA: The MITRE Corporation)

Gibson, G.G., et al., 1990, SPIE, 1299, 253

Goode, P.R., 1995, ESA, SP-376, 121

Goode, P.R., Qiu, J., Yurchyshyn, V., Hickey, J., Chu, M.C., Kolbe, E., Brown, C.T., Koonin, S.E., 2001, Earthshine observations of the earth's reflectance, *Geophys. Res. Lett.*, 28 (9), 1671-1674.

Intergovermental Panel on Climate Change (IPCC), 1992, Climate Change 1992, Suppl. Rep IPCC Sci. Assess, ed. J.T. Houghton, B.A. Callender, S.K. Varney, Cambridge, MA: Cambridge University Press.

Intergovermental Panel on Climate Change (IPCC), 1995, Climate Change 1994, Radiative Forcing of Climate Change and an Evaluation of the IPCC 1992 Emission Scenarios, ed. J.T. Houghton, L.G. Meira Filho, J. Bruce, H. Lee, B.A. Callender, E. Haites, N. Harris, K. Maskell, Cambridge, MA: Cambridge University Press.

Lockwood, M., 2002, private communication.

Rossow, W. B., A. W. Walker, D. E. Beuschel, and M. D. Roiter, International Satellite Cloud Climatology Project (ISCCP): Documentation of New Cloud Datasets. *WMO/TD-No. 737*, 115 pp, World Meteorological Organization, Geneva, 1996.

This manuscript was prepared with the AAS LaTeX macros v4.0.